SHADOWGRAPH FLOW VISUALIZATION OF ISOLATED TILTROTOR AND ROTOR/WING WAKES

Alexandra A. Swanson
Research Engineer
Sterling Software
Moffett Field, CA

Jeffrey S. Light
Research Engineer
NASA Ames Research Center
Moffett Field, CA

ABSTRACT

Shadowgraph flow visualization images were acquired from a 0.184-scale tiltrotor and wing in hover. Measurements and details of the vortex core structure were examined as a function of thrust condition and wake age. Experimental data for the isolated rotor wake geometry and rotor wake interactions with a semi-span wing and image plane were acquired. Quantitative measurements and comparisons of wake geometry and distortion were made for three configurations: the isolated rotor, rotor/wing, and rotor/wing/image plane. Comparisons between tiltrotor and helicopter rotor wake geometry measurements were made. Experimental wake geometry data were also compared with two wake models. Suggestions for improvements to existing prescribed-wake and free-wake models are proposed.

NOMENCLATURE

CR	camera/strobe distance to rotor centerline, ft (m)
C_T/σ	rotor thrust coefficient normalized by solidity
FM	figure of merit
h/R	normalized wing height from the rotor plane
r_v	radial distance from vortex core center, ft (m)
r_c/c	tip vortex core radius normalized by blade tip chord length
R	rotor radius, ft (m)
RS	rotor distance to screen, ft (m)
r/R	normalized radial distance from rotor centerline
t_1	instant of time, sec
V_θ	vortex core tangential velocity, ft/sec (m/s)
z/R	normalized axial distance from tip path plane
α_w	wing angle of attack, deg
δ_f	flap angle, deg
Γ_{TV}	tip vortex circulation, ft^2/sec (m^2/s)
σ	rotor thrust-weighted solidity
θ_{TW}	blade twist, deg
Ω	rotor speed, rad/sec
Ψ_b	blade azimuth location, deg
Ψ_w	wake age, deg

INTRODUCTION

The three-dimensional wake structure of a rotorcraft in hover and forward flight must be thoroughly analyzed to accurately predict rotor performance and dynamics. The rotor wake interactions with the airframe and blade/vortex interactions must also be considered for vibration, airload, and acoustic predictions. High resolution flow visualization methods can be used to obtain useful information for the development and validation of accurate mathematical wake models for loads predictions and acoustic research.

Presented at the 48th Annual Forum of the American Helicopter Society, Washington, D.C., June 3-5, 1992.

Flow visualization and wake geometry measurements for tiltrotors have not been as extensive as the work completed for helicopters. Reference 1 acquired tiltrotor wake geometry for a full-scale composite XV-15 Advanced Technology Bladed (ATB) rotor. Humidity conditions during this outdoor test were excellent for conducting flow visualization. The wake contraction of the XV-15 Advanced Technology Bladed tiltrotor was found to be greater than that of conventional helicopters (which were extensively documented in Refs. 2 and 3). Smoke flow studies of a 0.658-scale V-22 rotor/wing/image plane (Ref. 4) clearly established the presence of the fountain effect. Subsequently, the wide-field shadowgraph technique was used to examine the wake of a small-scale tiltrotor (Ref. 5). It was found that the wake contracts faster on the wing spar side of the rotor, but as the wake approaches the spar, a wake expansion takes place. Reference 6 is a study of the detailed structure of the fountain effect of a 1/12-scale full-span dual rotor model tiltrotor. Neutrally buoyant helium soap bubbles were used to study the unsteady flow qualities that give rise to strong time varying noise. Two regions of major recirculation were found: 1) the fountain regions between the two main rotors, and 2) an unsteady recirculating flow along and above the length of the fuselage.

Results are presented from a recent shadowgraph test which was conducted to obtain wake geometry of the V-22 tiltrotor. The vortex core structure and the relationship between core measurements and their sensitivity to thrust and wake age are examined. Discussion includes examination of the experimental tiltrotor wake in the presence of a semi-span wing and image plane. Additionally, experimental wake geometries of the isolated V-22 tiltrotor are compared with conventional helicopters, tiltrotors, and existing wake models.

EXPERIMENTAL SETUP

Model Description

An aerodynamically 0.184-scaled V-22 tiltrotor was tested at the NASA Ames Outdoor Aerodynamics Research Facility (OARF). Figure 1a shows the test installation for the shadowgraph flow visualization experiment.

Figure 1a. Shadowgraph test installation at the Outdoor Aerodynamic Research Facility

This rotor was mounted onto a hover test rig developed at NASA Ames. The wing support system was designed to mount above the rotor, with the rotor thrusting down and the wake traveling up into the wing. An 8-ft by 8-ft (2.4-m by 2.4-m) image plane was suspended from the model support structure, independent of the wing support, to simulate the centerline of a tiltrotor aircraft (no semi-fuselage was used). A 0.28-scale XV-15 wing with a variable flap was suspended from the wing support system. Figure 1b illustrates the rotor, wing, and image plane geometry. Complete rotor characteristics are given in Table 1 and the wing and image plane geometry are given in Table 2.

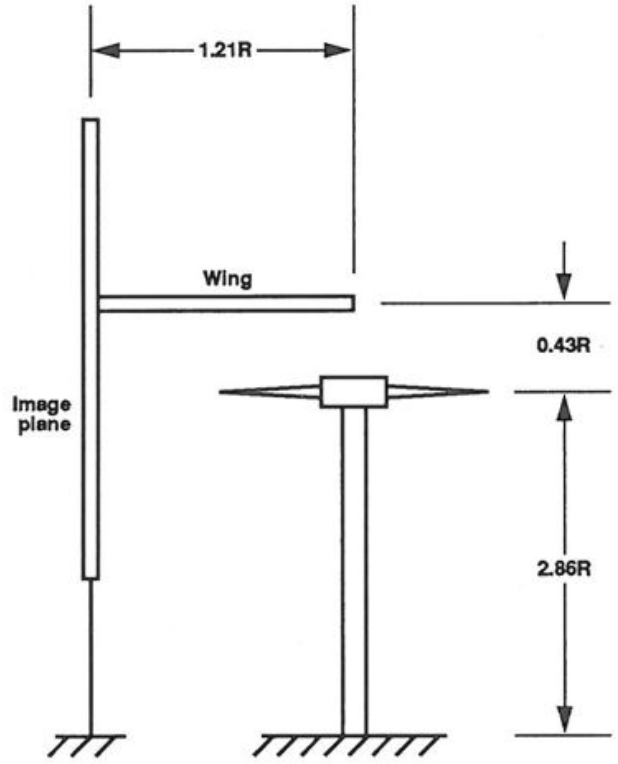

Figure 1b. Rotor, wing, and image plane geometry

Table 1. 0.184-Scale V-22 Rotor Characteristics

Number of blades	3
Rotor radius	3.5 ft (1.07 m)
Mean blade chord	0.45 ft (0.14 m)
Chord length at blade tip	0.37 ft (0.11 m)
Rotor solidity (thrust weighted)	0.1144
Blade twist	–34.08°
Blade precone angle	0°
Blade airfoils	XN-28, XN-18, XN-12, XN-09
Design tip speed	770 ft/sec (235 m/s)

Table 2. Wing and Image Plane Geometry

Wing airfoil section	NACA 64A223
Wing chord	1.47 ft (0.45 m)
Wing thickness ratio	23%
Wing twist, dihedral, sweep	0°
Flap chord ratio	30%
Distance from wing chord line to rotor hub	1.51 ft (0.46 m)
Wing span from rotor center line to image plane	4.22 ft (1.29 m)
Rotor cant angle relative to image plane	0°
Image plane size	8 ft. × 8 ft (2.4 × 2.4 m)

Flow Visualization Method

The wide-field shadowgraph flow visualization technique, reported in Refs. 5 and 7, was used to acquire images of the V-22 wake. Shadowgraph flow visualization was conducted with the use of still cameras, video cameras, strobes and retroreflective screens. Shadowgraphs were acquired by flashing the point source strobe through the the wake of the rotor operating in low ambient light conditions. The imaging device was focussed on the retroreflective screen to view the vortex shadows. Shadows of the wake were cast onto a screen and were reflected back to the imaging device and captured as photographs and video images. The shadows of the tip vortices were made visible by changes in the refractive index of the air caused by naturally occurring density gradients in the tip vortex cores (Ref. 8). Figure 2 is an example of a typical shadowgraph acquired in this test. The tip vortices are visible as thin dark spirals emanating from the blades. All shadowgraphs of the rotor wake were taken with the rotor thrusting down, and the wake traveling up.

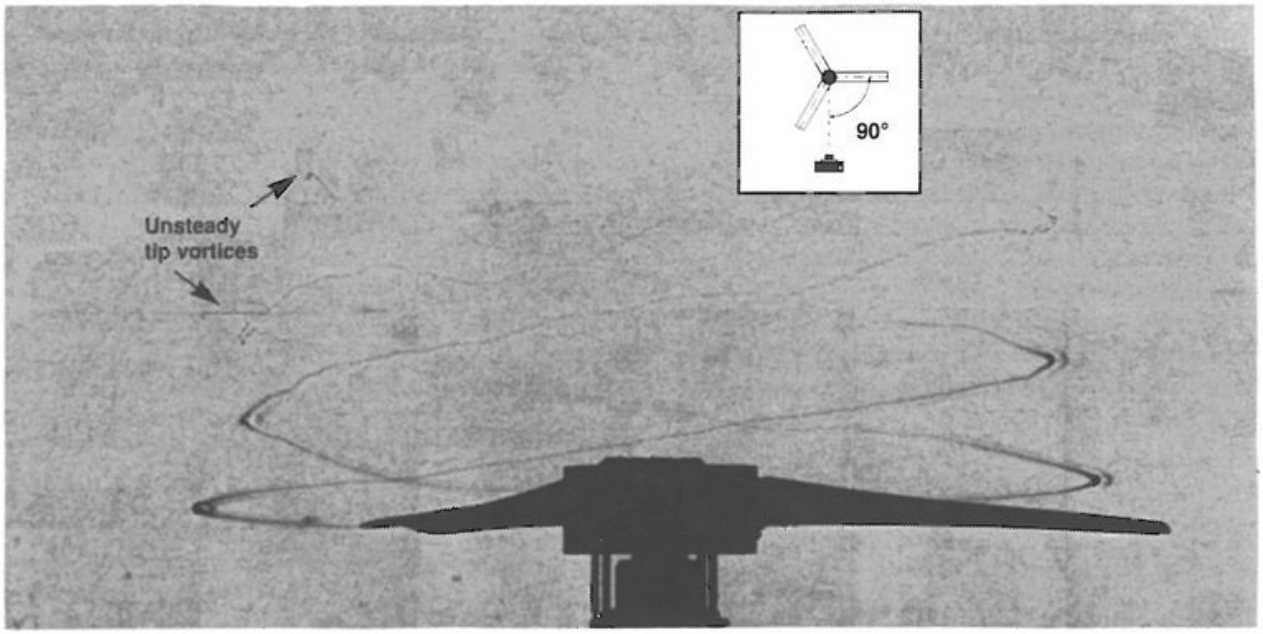

Figure 2. Shadowgraph of 0.184-scale isolated V-22 tiltrotor

Tip vortex visibility and details of the vortex core were examined at different camera to rotor (CR) and rotor to screen (RS) distances. For the isolated rotor and the rotor/wing configurations, only one view was acquired. Shadowgraphs for two views were imaged to study the three-dimensional nature of the rotor wake in the presence of the wing and image plane. For this case, the retro-reflective sheeting was applied to the image plane. Two strobes were flashed simultaneously through the rotor wake and images were captured simultaneously by two imaging devices.

Configurations and Test Conditions

Figures 3a-3c show schematics of the wide-field shadowgraph experimental setup for the three configurations that were examined. Two orthogonal views were imaged for studying the complex three-dimensional wake structure of the rotor in the presence of a semi-span wing and image plane (Fig. 3a). The image plane was removed in order to examine the effect of the presence of the wing only on rotor wake geometry (Fig. 3b). And finally, isolated rotor shadowgraphs were obtained with the wing and support structure completely removed (Fig. 3c). Testing occurred from midnight to dawn for two reasons: 1) the early morning hours are best for minimum wind conditions at the Outdoor Aerodynamics Research Facility, and 2) the shadowgraph technique requires low ambient light conditions. All shadowgraph testing occurred when wind conditions were less than 3.2 knots. These configurations and test conditions are given in Table 3.

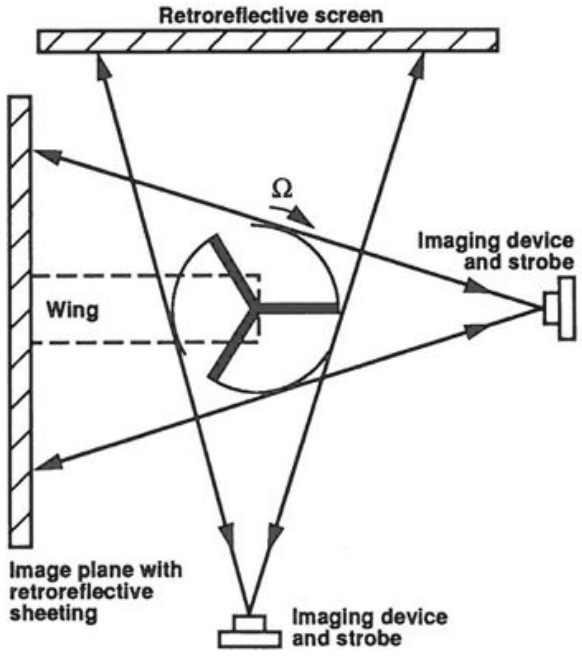

Figure 3a. Shadowgraph experimental set-up—rotor/wing/image plane configuration

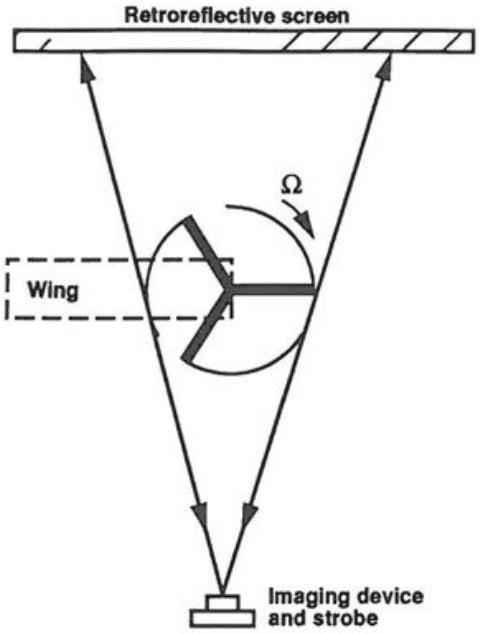

Figure 3b. Shadowgraph experimental set-up—rotor and wing configuration

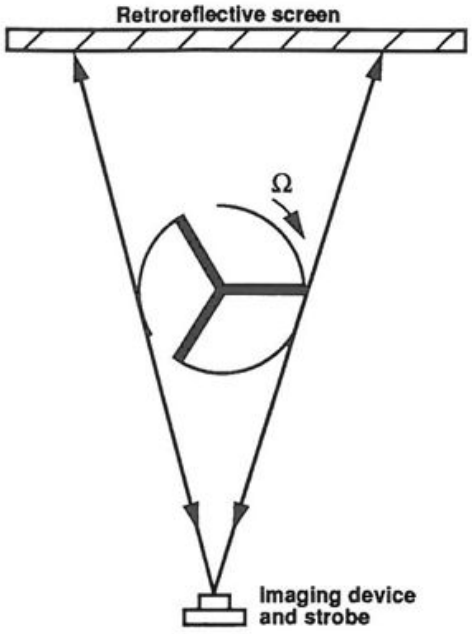

Figure 3c. Shadowgraph experimental set-up—isolated rotor configuration

Table 3. Configurations and Test Conditions

	Isolated Rotor	Rotor/Wing	Rotor/Wing/Image Plane
Tip Mach number	0.686	0.686	0.686
Collective	5°,6°,7°,8°,9°, 10°,11°,12°,13°	13°	5°,7°,9°,11°,13°
C_T/σ	0.050 to 0.146	0.143	0.043 to 0.139
C_T	0.0057 to 0.0167	0.0164	0.0049 to 0.0159
Wing flap angle	—	75°	65°, 75°
Wing incidence angle	—	0°	10°, 0°, –10°
Wind conditions	0.9 to 3.2 kts (0.46 to 1.65 m/s)	0 kts (0 m/s)	0.7 to 3.0 kts (0.36 to 1.54 m/s)
Camera to rotor distance	30 ft (9.14 m)	19.7 ft (6.0 m)	19.7 ft., 6.7 ft (6.0 m, 2.04 m)
Rotor to screen distance	10 ft (3.05 m)	13.3 ft (4.05 m)	13.25 ft., 4.3 ft (4.04 m, 1.31 m)

RESULTS

Double Image Phenomena

Figure 4 is an example of a close-up shadowgraph. It appears that two tip vortices are emanating from the same blade. However, it has been concluded that ambient humidity enabled direct viewing of the actual tip vortices as well as the shadowgraph images. The actual tip vortices and the shadowgraph of these tip vortices appear on most of the images for up to 2 or 3 blade passages. The focussed shadow of the tip vortex on the retroreflective screen is visible due to the density gradients within the tip vortex core. The actual tip vortex (which is not in focus) is visible due to the humidity content of the air when this test was conducted. The relative location of the unfocussed, or actual tip vortex, is consistent with strobe location relative to the camera (i.e. if the strobe was positioned to the right of the camera, the unfocussed image was to the right of the focussed shadow and vice versa). The actual spacing of the double image is consistent with the offset distance between the strobe light and camera device. The offset angle was less than 0.5° for shadowgraphs showing the whole rotor, while the close-up side views had offset angles as large as 2°. Figure 5 illustrates how the light rays from the point source strobe produce this double image effect. The offset angle between the camera and the strobe has been exaggerated in the figure for clarity.

Humidity measurements ranged between 65% and 80% during this test. The double image effect had been seen in only one other shadowgraph test, where humidity conditions reached as high as 68% (Ref. 9). Typically, only the shadow of the wake has been visible in shadowgraph tests previously conducted at NASA Ames Research Center. The climate conditions were reviewed for the XV-15 Advanced Technology Bladed tiltrotor test, where humidity enabled flow visualization studies of the tip vortices (Ref. 1). Humidity conditions in that test were consistently between 80% and 85%.

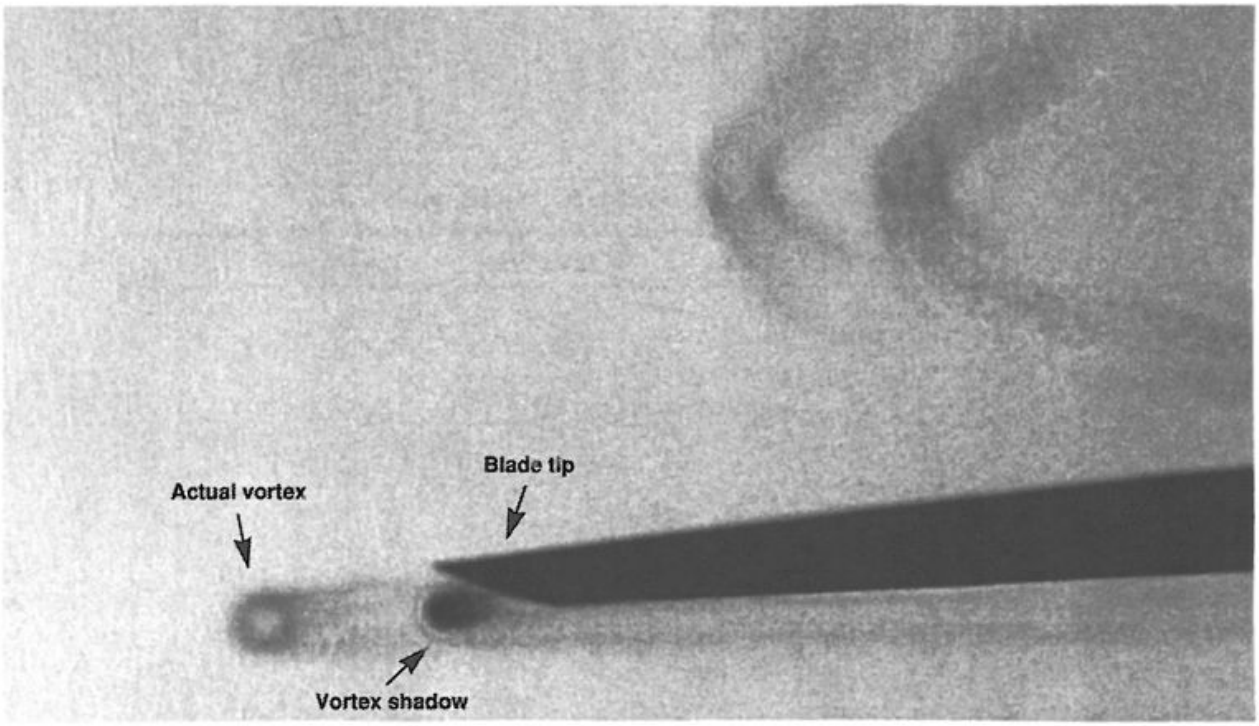

Figure 4. Detail of vortex core structure trailing off blade tip, $\Psi_w = 10°$

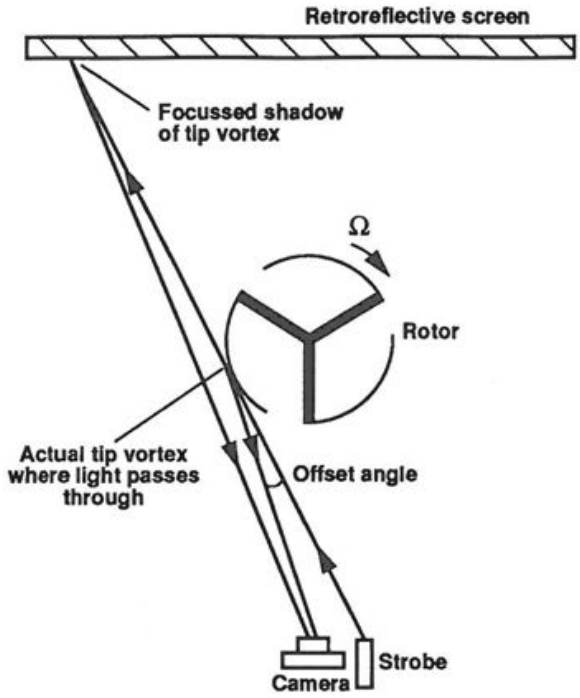

Figure 5. Double image effect of tip vortex produced by strobe offset

In addition to humidity, the retroreflective screen material also determines whether the actual tip vortex will be visible or not. A comparison was recently made between three different retroreflective screens (3M Scotchlite 7615, 7610, and 580-10) to determine which provided the most detail. The high contrast and the high gain retroreflective sheeting yielded similar results: both the tip vortices and shadows of the tip vortices were visible given the appropriate conditions. The white retroreflective sheeting did not provide enough contrast to see the actual tip vortices. A visibility check was conducted to further examine this phenomena by sweeping through collectives settings from 5° to 13° ($C_T/\sigma = 0.050$ to 0.146). The actual wake was visible only at thrusts greater than $C_T/\sigma = 0.113$. To summarize, the double image effect occurred when all of the following conditions were met: 1) humid conditions; 2) large bound circulation - high thrust condition; and 3) high contrast retroreflective sheeting.

Vortex Core Structure

Improved wake modeling will only be possible with detailed knowledge of not only the location, but also the size and structure of the vortex core. Vortex core modeling plays a significant role in predicting the wake induced velocity which influences blade loading (Ref. 10). Typically, laser velocimetry (LV) and hot wire techniques have been used to locate the tip vortex, investigate its structure, and determine core size (defined as the radial location of maximum tangential velocity). Both techniques have drawbacks, however. Hot-wire probes must be inserted in the flow and their presence may affect measurements. Laser velocimetry requires seeding the flow and long data acquisition times that make it difficult to examine the unsteady flow qualities. If the shadowgraph technique proves to be an accurate means of measuring core size, it would be very beneficial because it is non-intrusive and allows instantaneous examination of the flow field.

To date, there are limited measurements of rotorcraft vortex core size and structure. In this test, quantitative shadowgraph measurements were made of the visible tiltrotor tip vortex core. This tip vortex is visible because of changes in the refractive index of air caused by the density gradients within the core. Velocimetry is needed to determine how this visible core corresponds to the point of maximum tangential velocity. Although no velocimetry was conducted, measurements from this test show there is strong evidence the vortex core is sensitive to thrust and wake age. Interesting details of the vortex filament structure will be discussed with a possible explanation as to their existence.

Figures 4, 6, and 7 are examples of the detail of the core structure that was visible at close range. For all three figures, both the actual tip vortex and the shadow of the tip vortex are visible. The shadowgraphs show various regions of density gradients within the vortex core. This type of detail was apparent only at close inspection (CR = 1.9 R and RS = 1.2 R). When the newly rolled up tip vortex trails off the blade ($\Psi_w = 10°$), only a dark inner region is visible (Fig. 4). This dark region is a result of large density gradients within the core. At a later wake age ($\Psi_w = 24°$), an outer structure is visible (Fig. 6). The dark inner core is now surrounded by a lighter region. This lighter region is surrounded by a darker outer ring, which apparently is a region of moderate density gradients compared to the inner core. The vortex structure was further examined in shadowgraphs taken at two different time intervals (Figs. 7a, b). Variations in the density gradient properties of the inner and outer core regions of the tip vortex are visible for the same wake age ($\Psi_w = 120°$). Evidence of vortex filament distortion is also apparent in these figures.

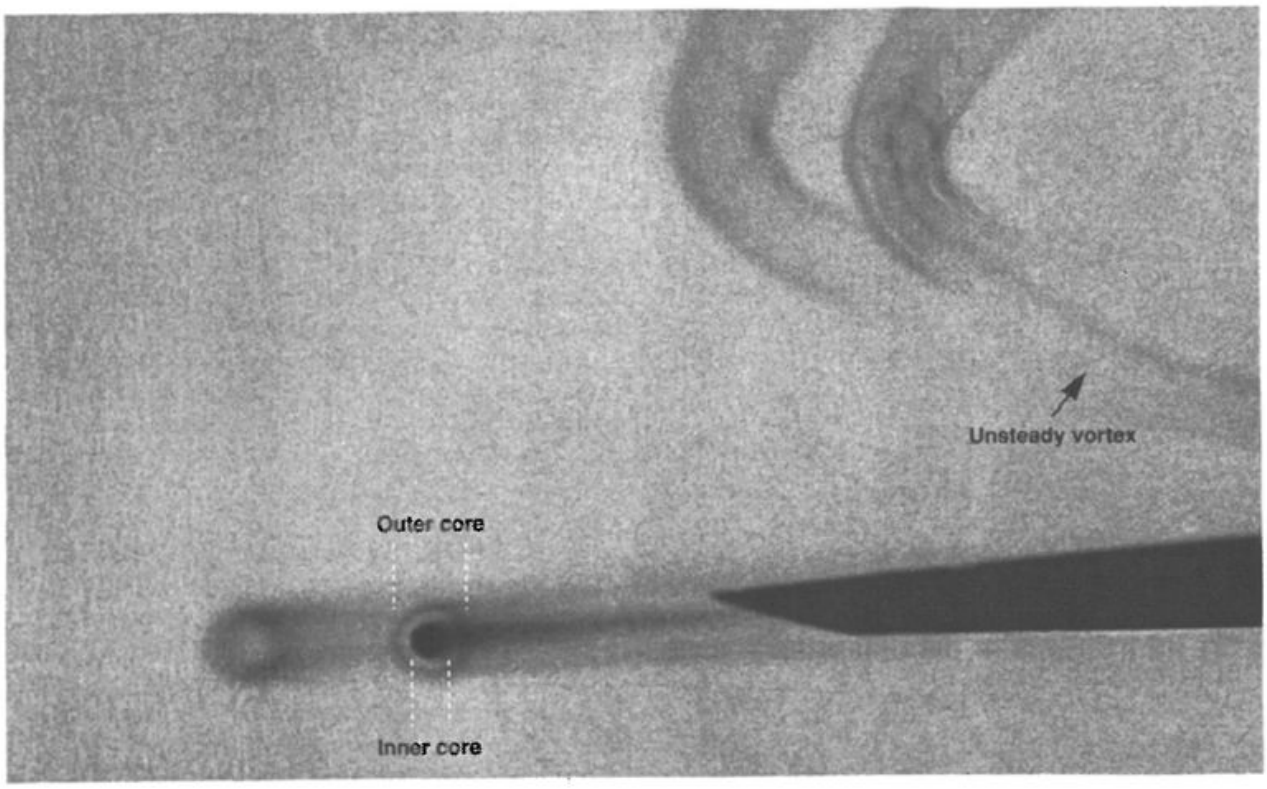

Figure 6. Detail of vortex core structure, $\Psi_w = 24°$

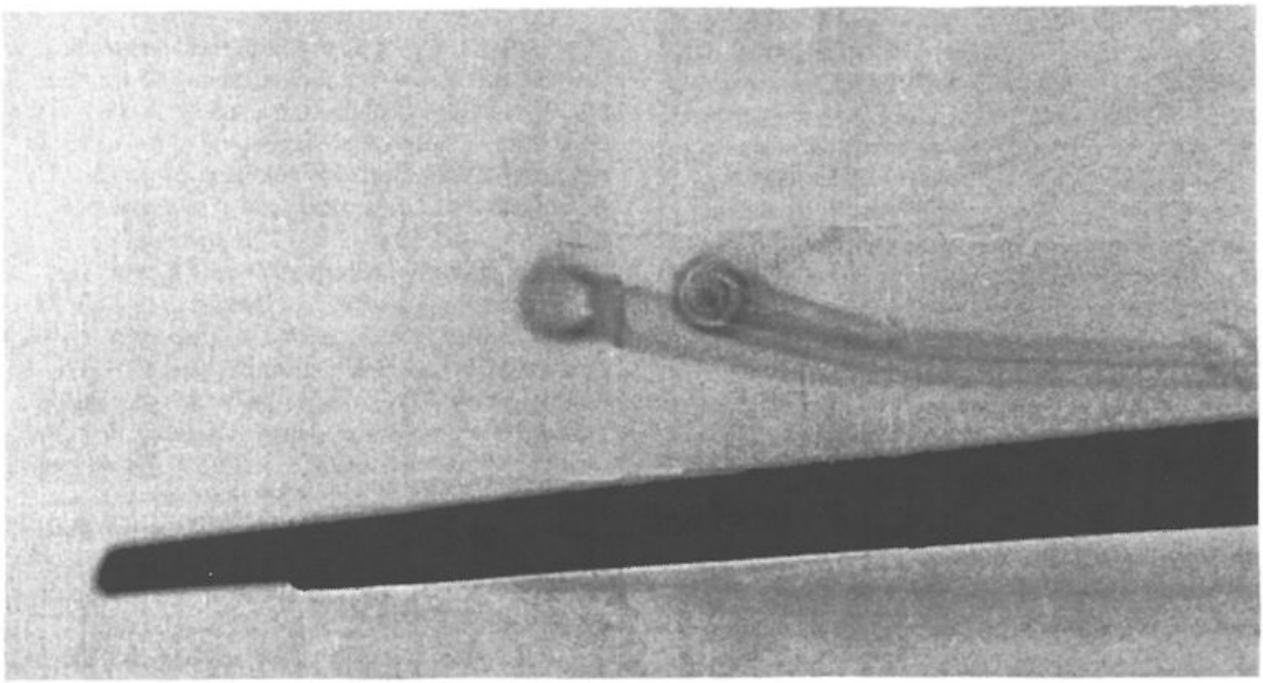

Figure 7a. Variations of vortex core structure at t_1

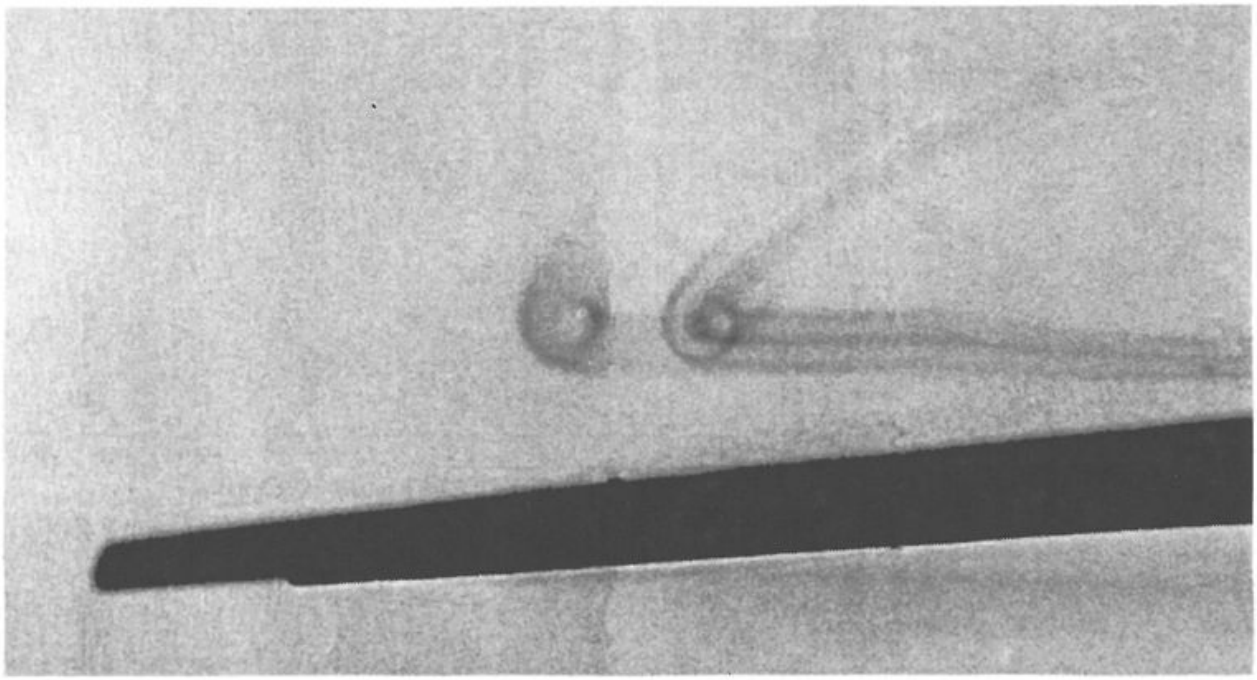

Figure 7b. Variations of vortex core structure at t_2

Previous work supports the observation that there are distinct regions of the vortex core. Perhaps the dark inner core is the viscous core where the circulation is proportional to the square distance of the core radius (Ref. 11); and the outer ring is the turbulent mixing region where circulation is a logarithmic function of radius (Refs. 12, 13). Reference 11 acquired velocity measurements from a model rotor (NACA 0012 airfoil, 8° linear blade twist) and found that the boundary between the viscous core and the turbulent mixing region occurs at $r_v/r_c = 0.75$; and the turbulent mixing region which extends to $r_v/r_c = 2.0$ is where r_v attains its maximum value. Shadowgraph results from this 0.184-scale V-22 tiltrotor test showed the ratio of the vortex inner to outer core measurement varied between 45% and 65%. On the average, the dark inner core radius was about 53% the size of the visible outer core radius.

All measurements cited in this paper were based on the shadow of the tip vortex as seen on the screen for the boundary or edge of the rotor wake. Previously, it has been suggested that distortions of the tip vortex could make the vortex core appear larger at the wake boundaries (Ref. 14). This is true when viewing the tip vortices from far distances. However, close-up shadowgraphs revealed that the outer tubal structure of the tip vortex is essentially the same throughout the tip vortex filament. Consequently, it is believed that the vortices, as viewed on the extreme boundary of the rotor wake, are not severely altered or distorted.

For one thrust condition and wake age ($C_T/\sigma = 0.139$, $\Psi_w = 50.8°$), core measurements were compared for two shadowgraph views: a full view of the rotor wake (CR = 8.6 R and RS = 2.9 R) and a close-up view of the rotor wake (CR = 1.9 R and RS = 1.2 R). Only an inner dark region of the tip vortex was visible for the larger camera and screen distances required for viewing the whole rotor wake. Comparisons of the tip vortex core measurements were made for the same thrust and wake age, but viewed from different distances. The closer view revealed a more visible and larger core structure that was 30% to 70% larger than that viewed from a further distance.

Shadowgraph measurements showed strong evidence that the vortex core is sensitive to thrust. Figure 8 shows the relative effect of thrust on the core measurements for one wake age ($\Psi_w = 50.8°$). An almost linear relationship exists between the core measurement and thrust condition. This means that for a full-scale V-22 hover condition ($C_T/\sigma = 0.128$), the vortex core radius would be about 12% of the chord. An expression was empirically derived that defines the shadowgraph core measurements as a function of thrust condition. The chord length at the blade tip was used to normalize the core radius measurements.

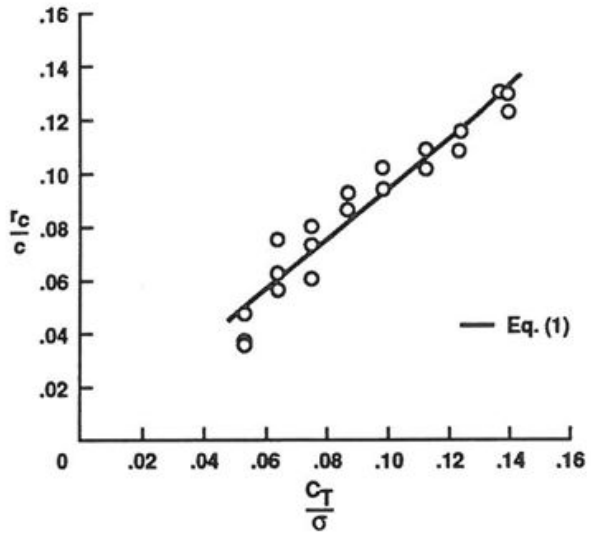

Figure 8. Tip vortex core measurements as a function of thrust coefficient

This expression is based on core measurements of the 0.184-scale V-22 tiltrotor for $\Psi_w = 50.8°$.

$$r_c/c = 9.25E\text{-}04 + 0.932C_T/\sigma \quad (1)$$

This relation holds for the thrust range, $0.053 < C_T/\sigma < 0.146$. As the blade stalls, a reduction in thrust would cause a reduction in the measured vortex core.

Shadowgraph measurements also showed strong evidence the vortex core is sensitive to wake age. Results showed the core radius increased with wake age (Fig. 9). An expression was empirically derived that defines the shadowgraph core measurement as a function of wake age. The following expression is based on core measurements of the 0.184-scale V-22 tiltrotor for $C_T/\sigma = 0.139$ and $0° < \Psi_w < 195°$ where Ψ_w is in radians.

$$r_c/c = e^{-2.15+0.094\Psi_w} \quad (2)$$

These measurements show the vortex core increases with age, which is an effect caused by viscous diffusion of the vortex. By the first blade passage ($\Psi_w = 120°$), the vortex core increased by 2% of the chord. By 195° of wake age, the core radius grew to about 16% of the chord in this region of the wake. This is considerably larger than the 10% value typically used for helicopter rotor analysis (Ref. 10).

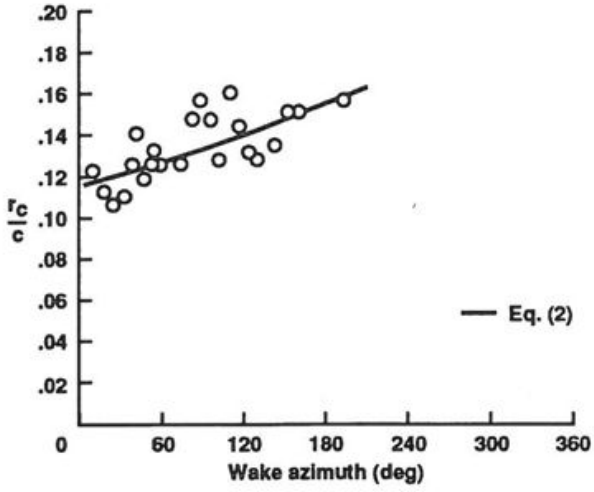

Figure 9. Tip vortex core measurements as a function of wake age

An attempt was made to predict the tangential velocity of the tip vortex based on the experimental measurements acquired in this test. Beddoes (Ref. 15) empirically derived an expression that estimates the vortex circulation strength:

$$\Gamma_{TV} = 2.4c\Omega RC_T/\sigma \quad (3)$$

Scully (Ref. 16) developed an expression that estimates the tangential velocity of the vortex core using a distributed vorticity model:

$$V_\theta = \Gamma_{TV}\, r_v/2\pi\left(r_v^2 + r_c^2\right) \quad (4)$$

By substituting Eq. (2) into Eq. (4), we arrive at an expression that estimates the maximum tangential velocity for a given wake age.

$$V_\theta = \Gamma_{TV}/4c\pi e^{-2.15+0.094\Psi_w} \quad (5)$$

If the assumption is made that the outer vortex core measurements acquired in this test correspond to the points of maximum tangential velocity, then the predicted tangential velocity of the vortex core, where $r_c/c = 0.12$, $\Psi_w = 50.8°$ and $C_T/\sigma = 0.139$, is about 170 ft/sec (51.8 m/s). Further studies using LV measurements in conjunction with flow visualization will better quantify interpretation of these shadowgraph core measurements. Such findings will help determine whether the wide-field shadowgraph technique should be used for future studies of the vortex core structure.

Wake Characteristics

Isolated Rotor. Figure 2 shows a shadowgraph of the isolated V-22 rotor taken at a $C_T/\sigma = 0.146$ with a wind speed of 1.7 knots. Tip vortices are visible as thin dark spirals trailing from the blades. The third and fourth tip vortices ($\Psi_w = 357°$, $\Psi_w = 476°$) on the left side of Figure 2 are very unsteady. Figure 10 shows another shadowgraph of the isolated rotor at a different blade azimuth location. The wake appears unsteady after one blade passage ($\Psi_w = 120°$). The tip vortex on the right side of the figure ($\Psi_w = 411°$) expanded after three blade passages. Similar shadowgraph results were found during a Lynx tail rotor test (Ref. 9) where the wake boundary contracted and then expanded after one complete rotor revolution ($\Psi_w = 360°$). Examination of videotapes of the 0.184-scale V-22 tiltrotor shows evidence that wake expansion occurs on both sides on the rotor, but it appeared to be more visible on the right side, with the blade approaching the camera. Review of Lynx shadowgraph images showed that the wake expansion was also more prevalent on the side of the rotor with the blade approaching the camera. There was no symmetry to the unsteady rotor wake expansion as observed in both tests. Further flow visualization should be done to study the wake boundaries from various azimuth perspectives (not just two sides) in order to better understand the unsteadiness of the wake and determine whether there is a periodicity to this phenomena.

Prior to examining the tip vortex geometry of the isolated rotor, shadowgraph images were first visually inspected for wake unsteadiness as a function of thrust. Figures 11a -11c show a sampling of three thrust conditions. Relatively consistent helical wake boundaries were found up to $C_T/\sigma = 0.099$ as shown in Figure 11a. However, at high thrust ($C_T/\sigma = 0.124$) vortex filament distortion was apparent. Instead of an ideal helical wake structure, Figure 11b shows a wavy helical wake structure. Figure 11c also shows the wake was sufficiently distorted at higher thrust ($C_T/\sigma = 0.140$), that the tip vortex was only visible for two to three blade passages. Perhaps the unsteadiness of the wake is due to portions of the blade span stalling. Typically, rotors with high solidities at high operating thrust conditions are susceptible to tip vortex induced stall. This could explain why the low thrust conditions have well-behaved helical wake structures. Another possible explanation of this unsteadiness at high thrust conditions is a periodic lateral whip-like motion where the wake after one complete rotor revolution begins to shift back and forth (left side to right side).

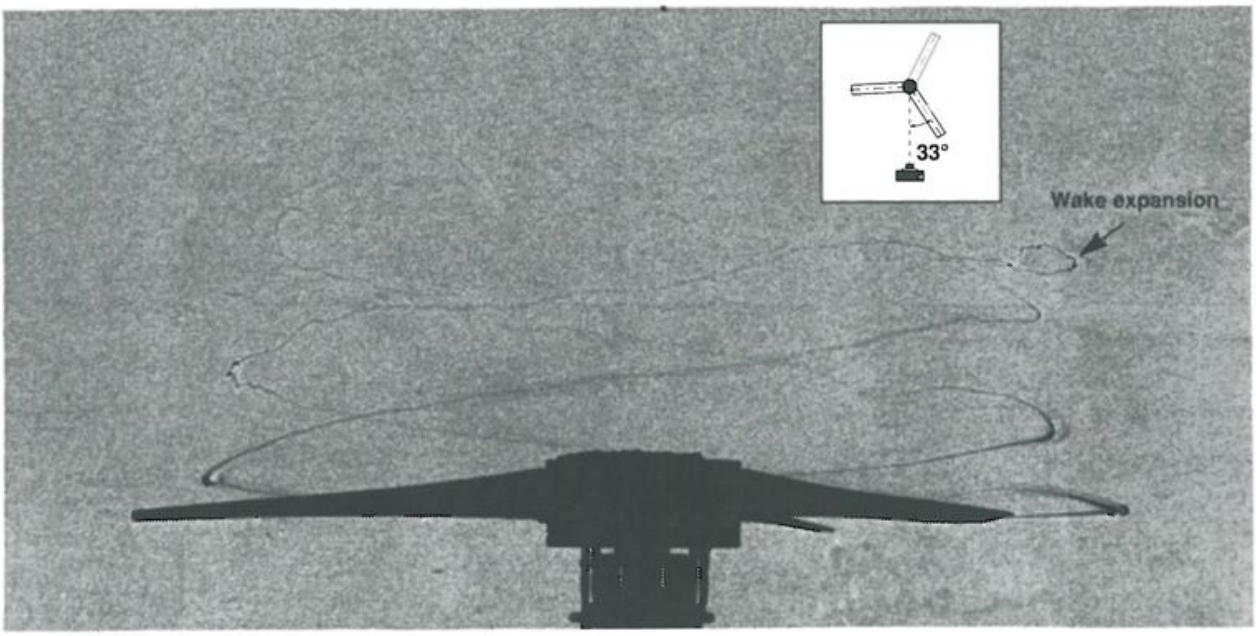

Figure 10. Isolated rotor with unsteady wake on right side on the rotor disk

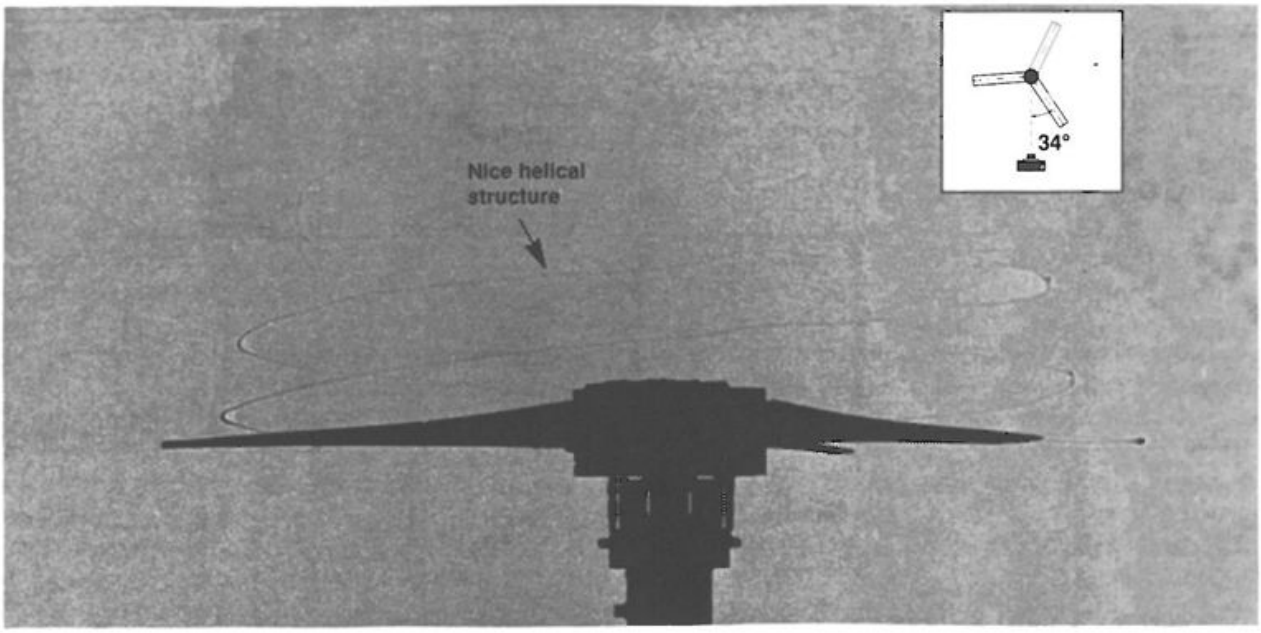

Figure 11a. Isolated rotor wake structure for 9° collective

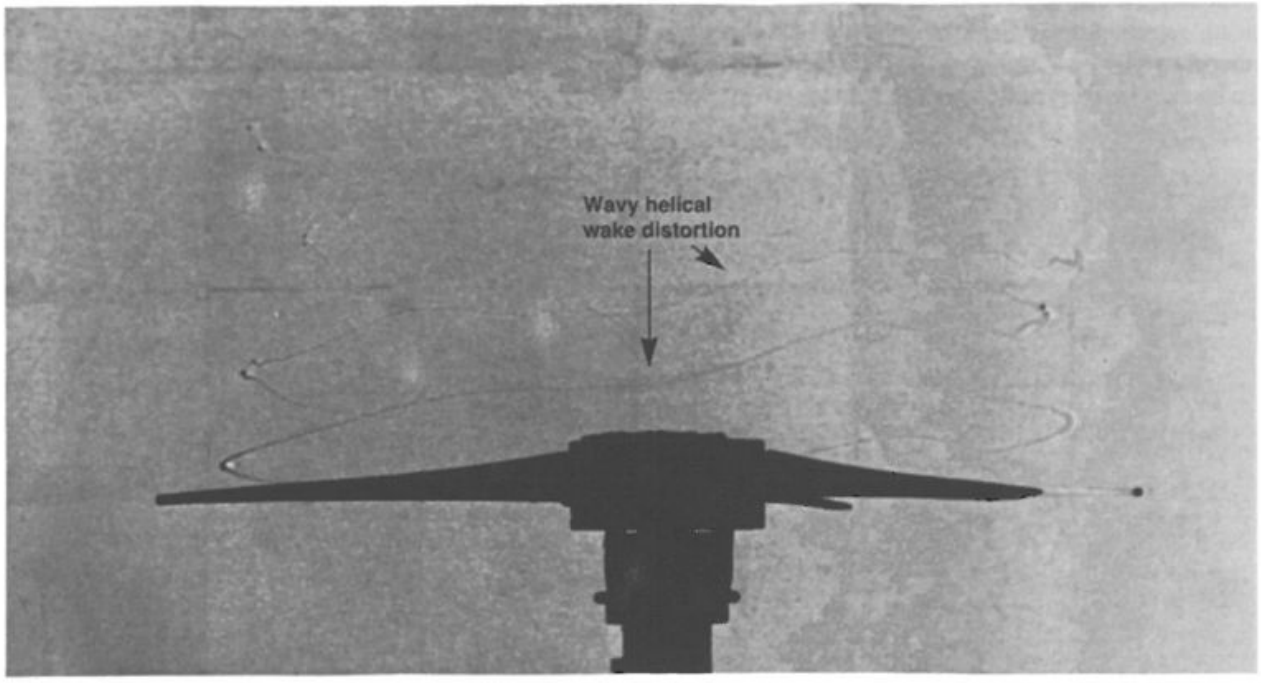

Figure 11b. Isolated rotor wake structure for 11° collective

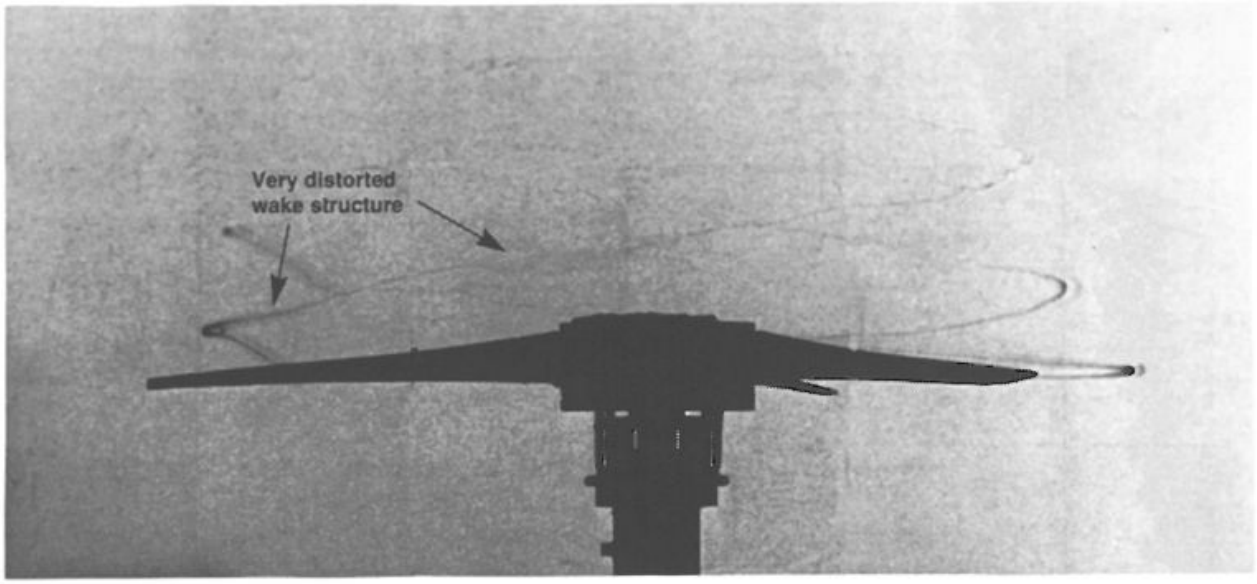

Figure 11c. Isolated rotor wake structure for 13° collective

Complete isolated wake geometry was acquired for three thrust conditions (C_T/σ = 0.099, 0.124, 0.146). Figures 12a and 12b show the unsteadiness of the axial and radial tip vortex coordinates for two thrust conditions (C_T/σ = 0.146, 0.099). There was a similar amount of scatter in the axial and radial wake geometry measurements for all three thrust conditions, with unsteadiness becoming apparent by the first blade passage (Ψ_w = 120°). As expected, Figure 12a shows that the axial descent rate of the tip vortices increases with increasing thrust. Figure 12b does not show any appreciable change in radial contraction for the thrust conditions examined. Both the axial and the radial wake boundaries are plotted for C_T/σ = 0.146 in Figure 13. This figure shows the varying unsteadiness between the left side and the right side of the rotor. Videotapes of shadowgraphs verified this unsteadiness. It was clear that the tip vortex distortion and wake boundary expansion were more apparent or visible on the side of the rotor where the blade approaches the camera.

Rotor and Wing. Shadowgraphs were acquired of the rotor and wing configuration at one thrust condition (C_T/σ = 0.142). Figure 14 is a typical shadowgraph for this configuration. Figure 15 shows the differences in axial and radial tip vortex coordinates with and without the presence of the wing. The presence of the wing had a minimal effect on the thrust for a given collective of 13°. The axial tip vortex coordinates were unsteady with the wing present (Fig. 15a). After the first blade passage (Ψ_w = 120°), the axial descent appears to be slightly greater than the isolated rotor up to Ψ_w = 180°. Thereafter, the tip vortex axial descent slows down as it approaches the wing. Figure 15b shows a more significant difference between the two configurations. The maximum radial contraction for the tip vortex located between the rotor plane and the wing was about 82% of the rotor radius and occurred about Ψ_w = 195°. This agrees with the results described by Reference 5, which indicates that the wing essentially acts as a ground plane.

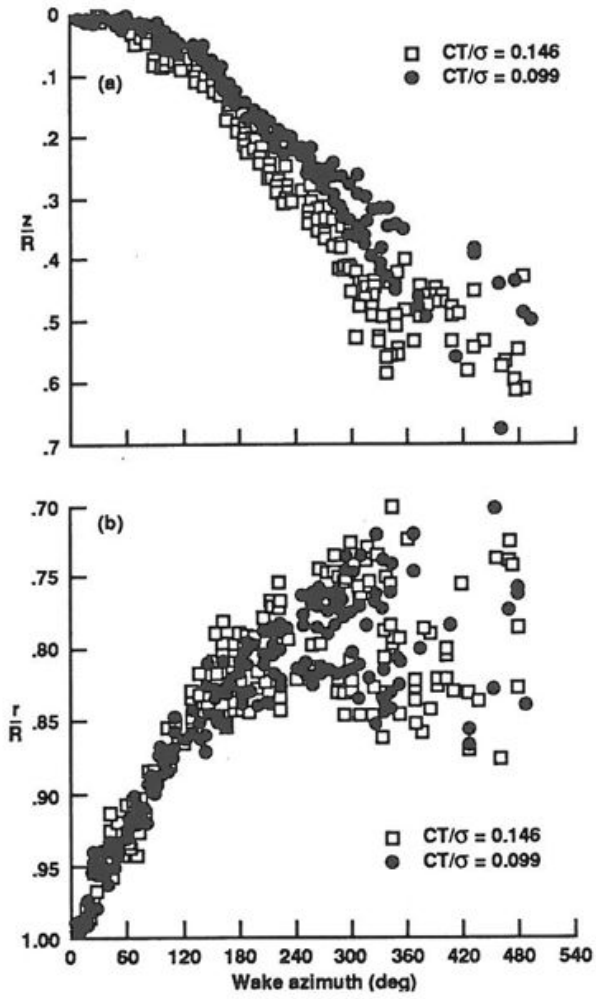

Figure 12. Wake geometry of isolated rotor for two thrust conditions; a) axial, b) radial

Rotor/Wing/Image Plane

Shadowgraphs for two orthogonal views of the rotor/wing/image plane configuration were obtained simultaneously. Figure 16 shows a shadowgraph obtained at a high thrust condition ($C_T/\sigma = 0.139$). From the spanwise view (Fig. 16a), unsteady tip vortices are apparent near the image plane. These vortices were considerably more unsteady than those seen in the rotor/wing configuration without the image plane (compare Fig. 14 with 16a). Two, and occasionally three, tip vortices were visible in the region between the rotor, wing, and image plane. Figure 16b shows a cross-sectional view of the wing and leading edge of the rotor disk. In this close-up view, the tip vortices were most visible near the extreme boundaries of the wake and again only about two tip vortices were visible. Perhaps the decrease in visibility of the tip vortex forward of the wing corresponded to a decrease in vortex strength due to the presence of the wing. Not much detail was seen in the region immediately adjacent to the wing, because the reflective quality of the screen was poor.

Figures 17 and 18 show the effect of the image plane on the wake geometry for one thrust condition ($C_T/\sigma = 0.139$). The data shown in Figure 17 is for the side of the rotor over the wing and adjacent to the image plane. The image plane reduced the thrust for a given collective of 13° by about 5%. Recirculation evidently affects the rotor inflow by reducing the effective angle of attack of the rotor. The axial tip vortex coordinates were very unsteady with both the image plane and wing present (Fig. 17a). Since variations in thrust conditions have little effect on the radial wake geometry of a rotor, meaningful comparisons between the rotor/wing and rotor/wing/image plane configurations were made. The radial tip vortex location was greatly affected by the addition of the image plane (Fig. 17b). There was a tremendous amount of fluctuation in the location of the tip vortex in close proximity to the image plane. With the wing and image plane installed, the radial wake boundary contracted to about 95% of the rotor radius before expanding along the wing. This maximum contraction occurred by the first blade passage ($\Psi_w = 120°$). Based on the trends of the tip vortex geometry measurements, it appears the radial wake boundary would encounter the image plane before the third blade passage ($\Psi_w = 360°$). Figure 18 shows both the radial and axial wake boundaries on the same plot. The isolated rotor wake geometry is superimposed to compare its wake boundary characteristics with the other two configurations. For the wing-only configuration, the wake boundary would appear to strike the wing at about the 100% radial position. However, with the image plane in place, the wake is very unsteady and expands towards the image plane giving evidence to the induced velocity recirculation known as the fountain effect. Reference 6 studied the spanwise flow, fountain height, and recirculating flow for a 1/12-scale full-span dual rotor model tiltrotor and found the recirculating flow fluctuates randomly from side to side. According to Reference 6, time varying properties of the flow cannot be adequately studied by one rotor and image plane due to the asymmetry of the fountain flow. Nevertheless, the current test provided useful data on flow recirculation and wake unsteadiness.

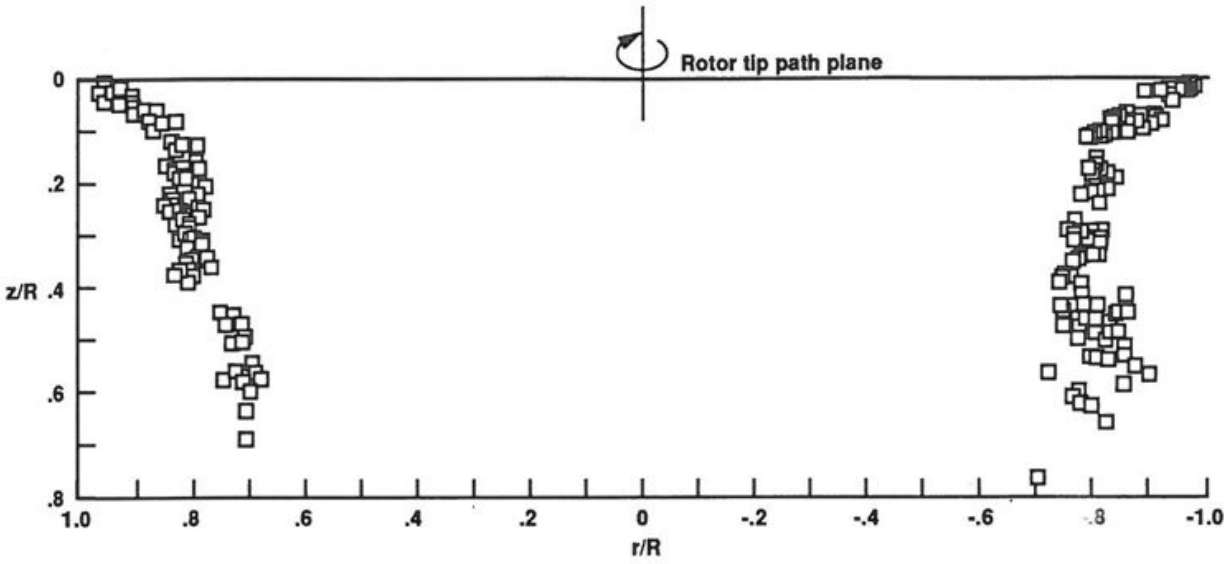

Figure 13. Wake boundaries on left and right side of isolated rotor at high thrust

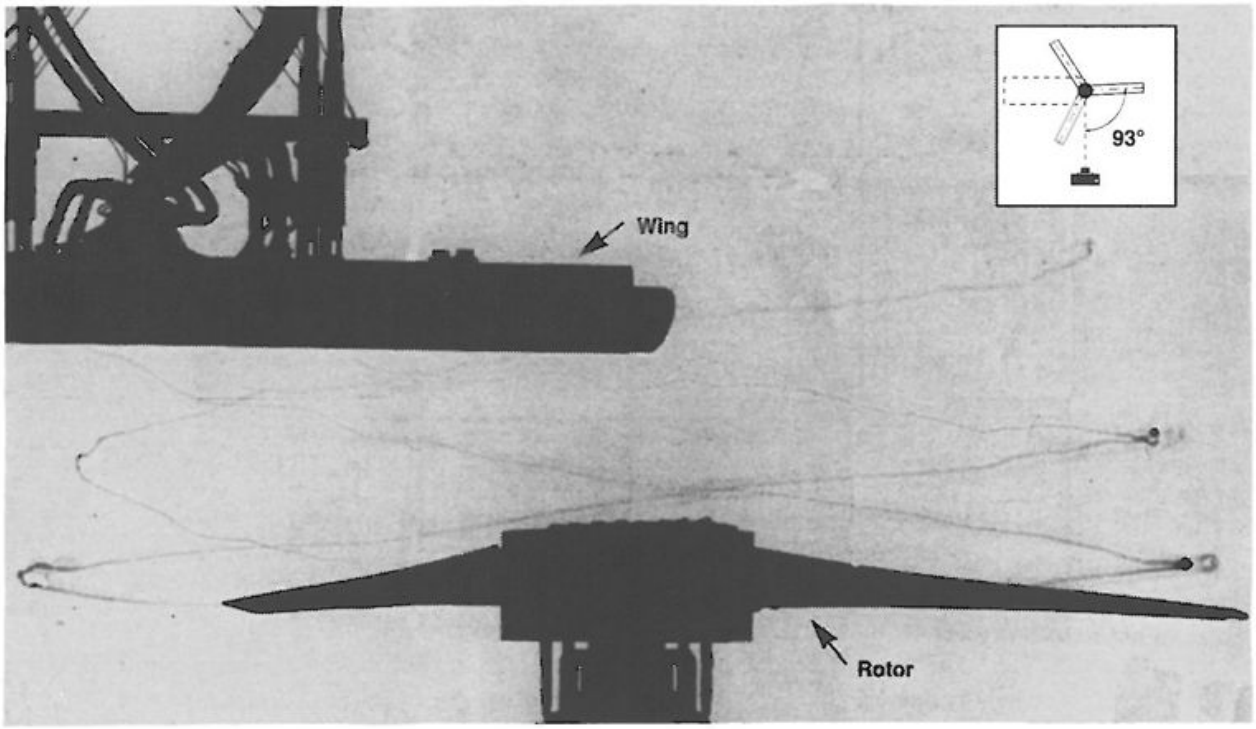

Figure 14. Shadowgraph of the rotor and wing configuration ($\delta_f = 75°$, $\alpha = 0°$)

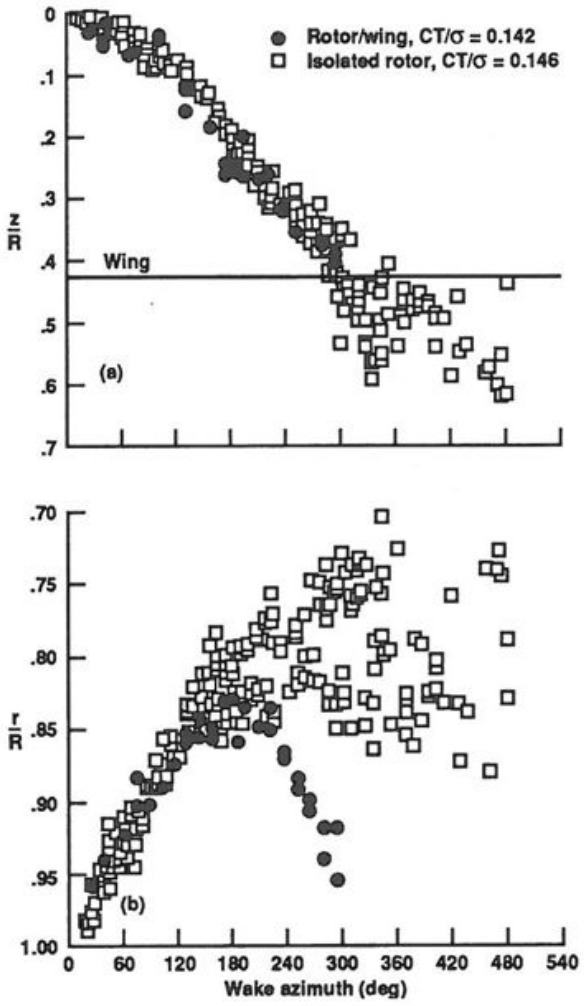

Figure 15. Effect of wing on wake geometry; a) axial , b) radial

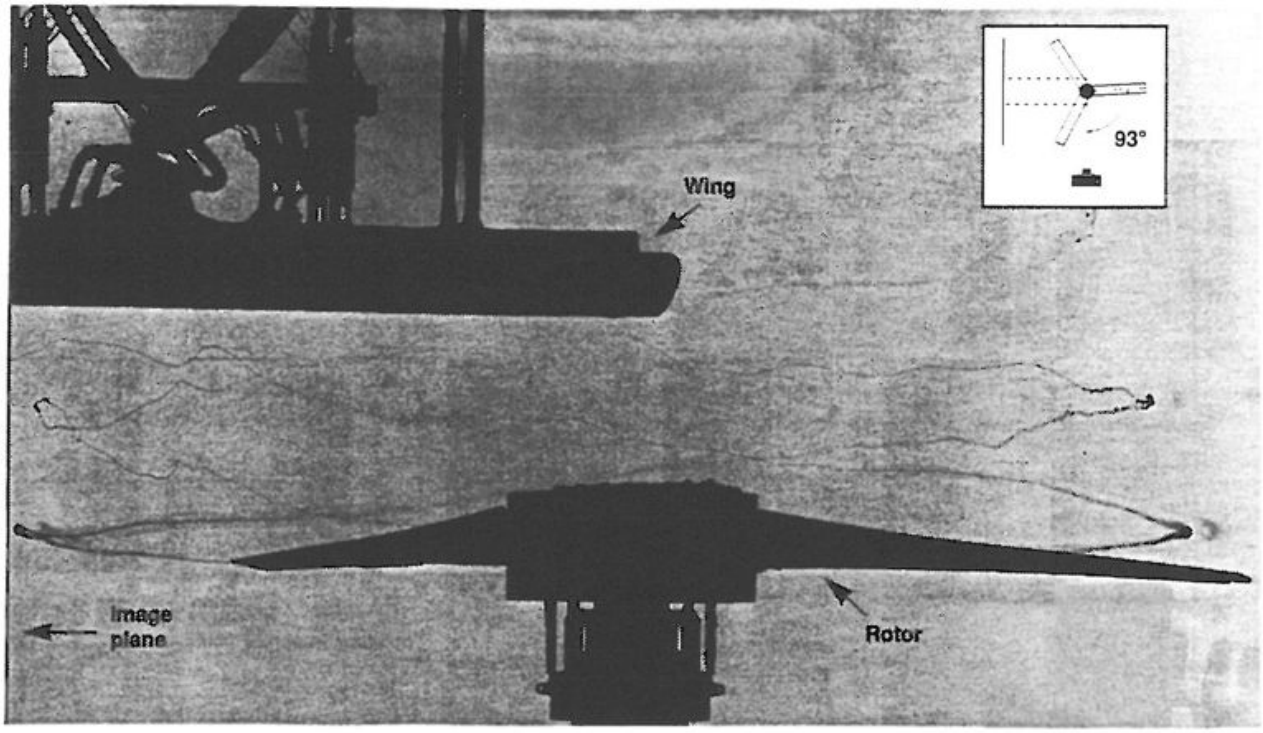

Figure 16a. Spanwise view of rotor, wing, and image plane configuration ($\delta_f = 75°$, $\alpha = 0°$)

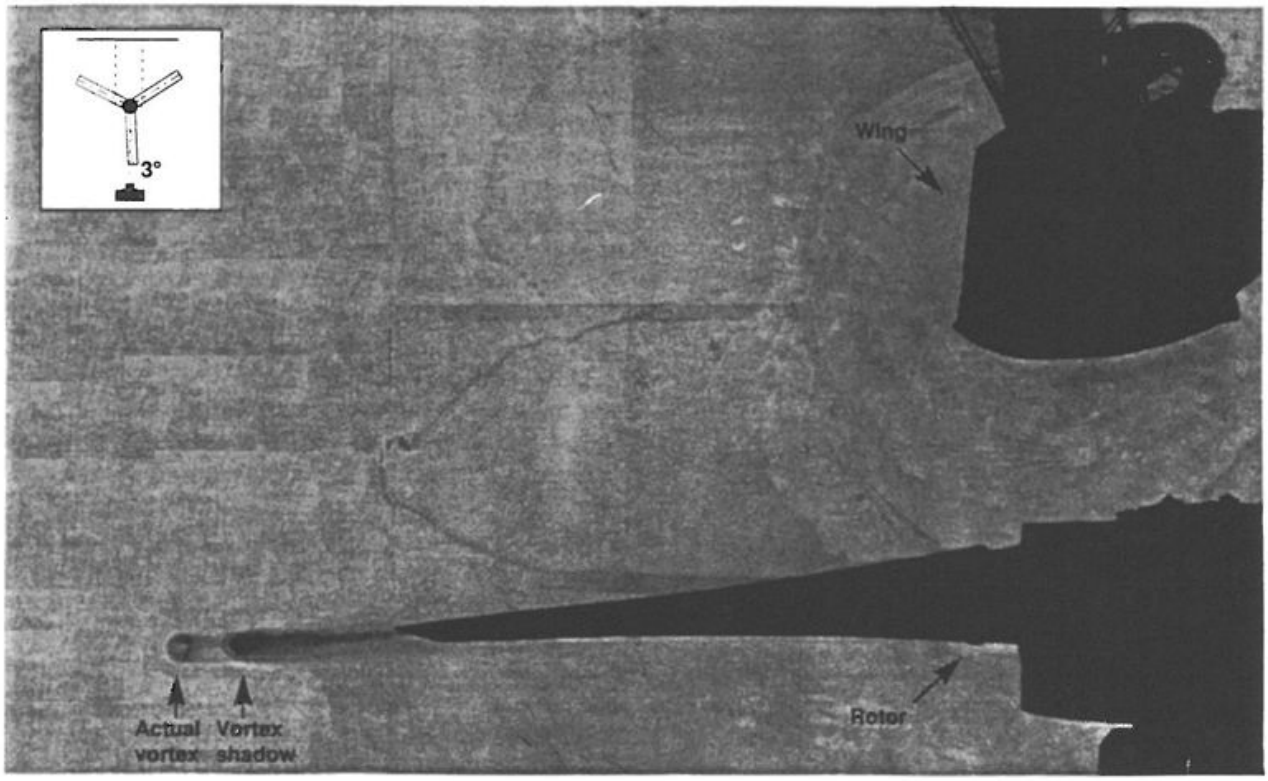

Figure 16b. Chordwise view of rotor, wing, and image plane configuration ($\delta_f = 75°$, $\alpha = 0°$)

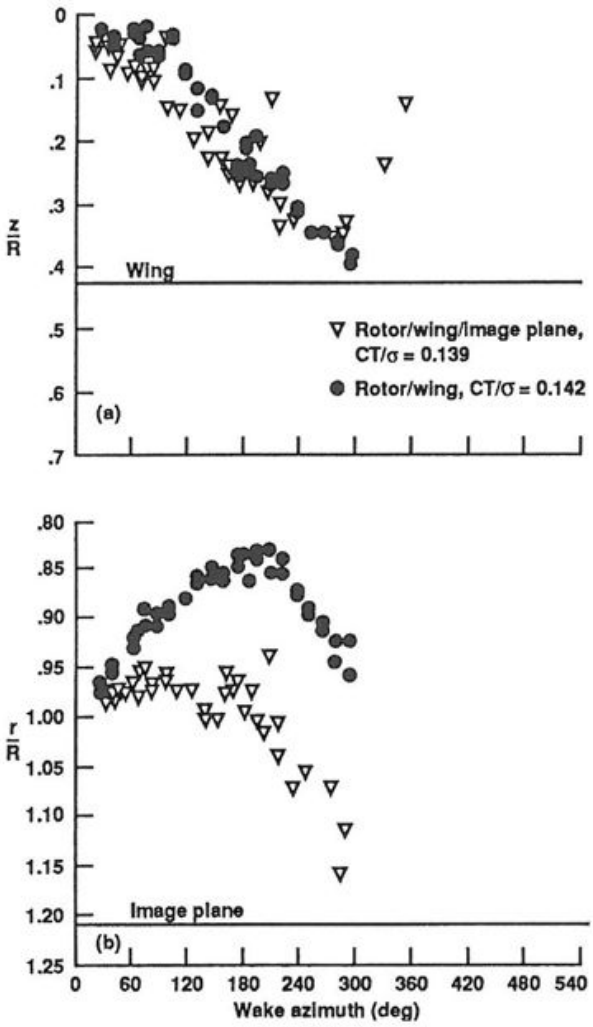

Figure 17. Effect of image plane and wing on wake geometry; a) axial, b) radial

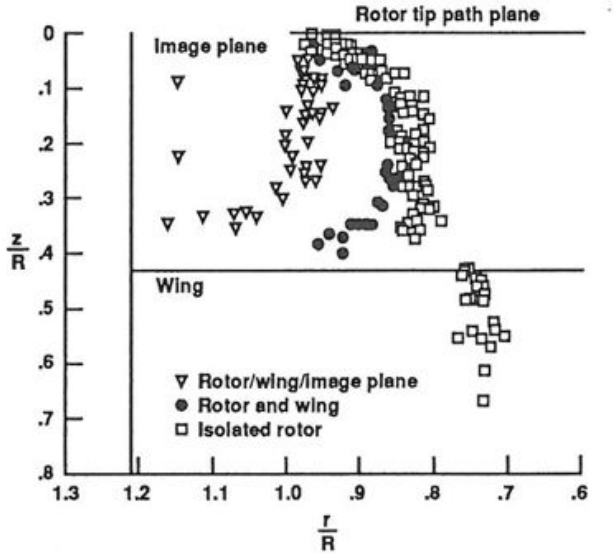

Figure 18. Axial and radial wake boundary comparisons for three configurations

CORRELATION EFFORTS

Isolated Rotor Wakes

Experimental wake geometry measurements of the 0.184-scale V-22 tiltrotor were compared with two other rotor systems: the Lynx tail rotor (Ref. 9)—no blade twist, and the XV-15 Advanced Technology Bladed tiltrotor (Ref. 1)—high blade twist. These comparisons were made in order to determine whether there were any radical differences between simple rotor systems and tiltrotors. The following are not identical comparisons and therefore, only general conclusions can be drawn due to the differences in model scale, blade number, solidity, and twist. References 2 and 3 were used to assess these variations in rotor characteristics, keeping in mind that such empirically derived predictions are based on rotors with no taper, linear blade twist, and low disk loadings.

Figure 19a shows that the axial descent rate of the untwisted Lynx rotor is greater than that of the highly twisted V-22 tiltrotor for a constant C_T. This is consistent with the Kocurek-Tangler prescribed wake theory. Figure 19b shows the radial contraction of the V-22 tiltrotor is greater than that of the Lynx rotor. Similar comparisons between tiltrotor and helicopter wake contractions were made in Reference 1. It is also interesting to note that both tiltrotors and conventional helicopters exhibit the same relative level of wake unsteadiness.

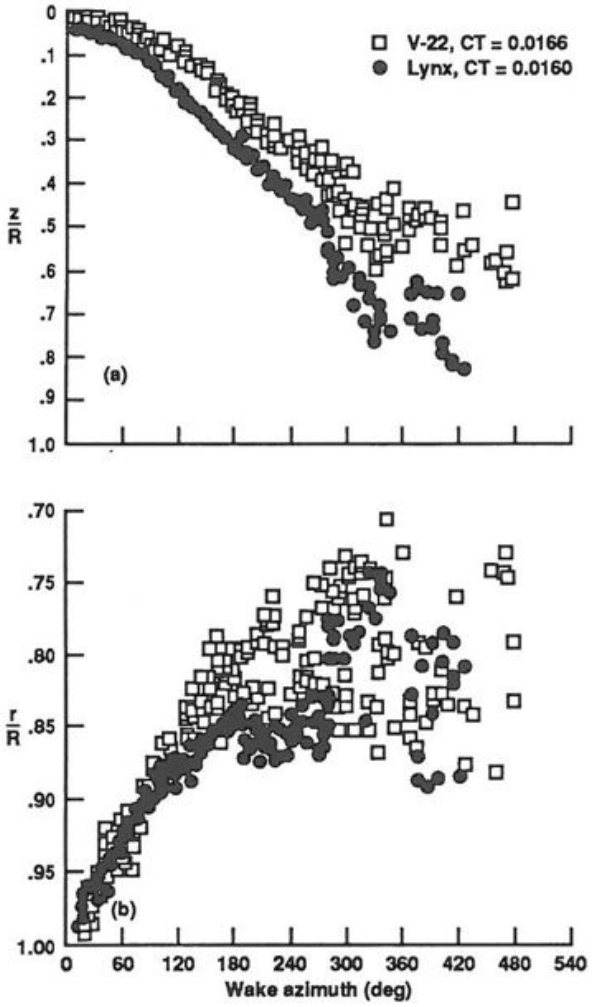

Figure 19. Comparison between V-22 and Lynx wake geometries; a) axial, b) radial

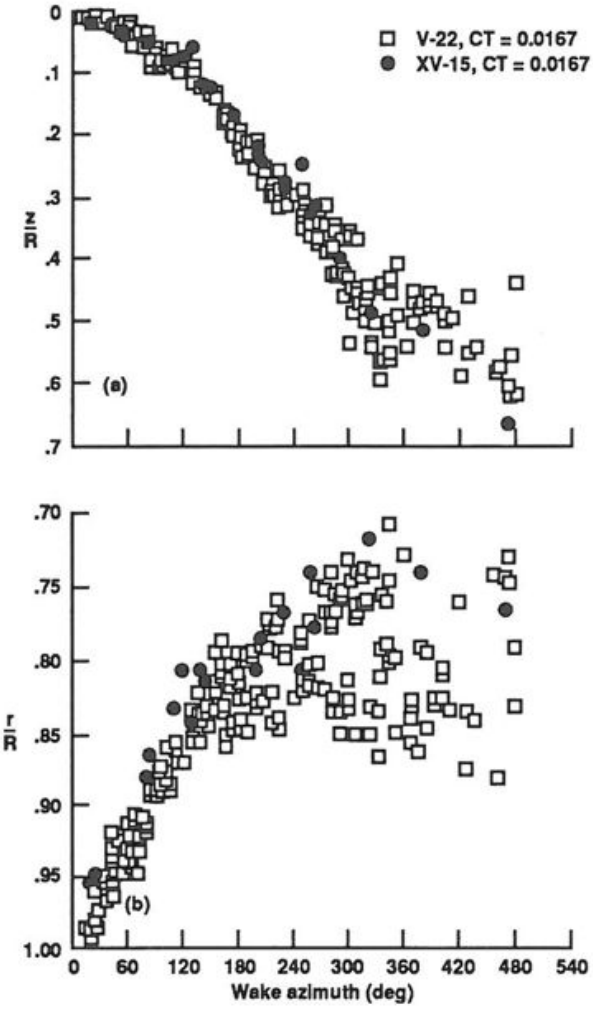

Figure 20. Comparisons between V-22 and XV-15 ATB tiltrotor wake geometries; a) axial, b) radial

Comparisons of the wake geometries of the two different tiltrotors are shown in Figure 20 for the same thrust ($C_T = 0.0167$). References 2 and 3 predict that a higher linear twist distribution results in a lower axial descent rate. Although the twist distribution of both tiltrotors are different (V-22 $\theta_{TW} = -34°$, XV-15 ATB $\theta_{TW} = -47°$), both exhibit nearly the same axial descent rate. The contraction rate of both tiltrotors are also similar. The slightly higher radial contraction of the XV-15 Advanced Technology Bladed tiltrotor may be due to differences in blade tips and twist distributions.

Differences between the experimental and predicted wakes of the isolated V-22 tiltrotor were examined. These shadowgraph measurements were compared with two different wake models. The first model is an empirical method based on the work of Kocurek and Tangler (Ref. 3). They experimentally determined the tip vortex geometry of a large set of rotors with different attributes (number of blades, solidity, twist, etc.) and developed an empirically prescribed wake. The Kocurek-Tangler prescribed-wake is based on linearly twisted blades. The value of twist that was used for the non-linearly twisted V-22 blades was the total twist over the length of the blade. The second tip vortex geometry model uses the EHPIC (Evaluation of Hover Performance using Influence Coefficients) free-wake analytical model (Refs. 17, 18). This analysis uses curved vortex elements and an influence coefficient method to obtain a force-free wake structure.

Comparisons of the radial and axial tip vortex geometry for the shadowgraph tip vortex measurements and wake models are shown in Figure 21 for $C_T = 0.0149$. The other two thrust conditions showed similar results. Both wake models essentially agree with the measured axial tip vortex geometry. Before the first blade passage ($\Psi_w = 120°$), both wake models slightly overpredict the axial descent of the tip vortex, while after the first blade passage, the Kocurek-Tangler model predicts a higher descent rate than EHPIC. The large axial displacement in the EHPIC wake just after the tip vortex leaves the blade has been seen in past studies, and is not yet completely understood (Ref. 19). Because of the unsteadiness in the tip vortices after two blade passages ($\Psi_w = 240°$) , it is difficult to determine which predicted geometry is best, but they both appear to predict the average axial tip vortex locations (Fig. 21a). The predicted and measured radial tip vortex geometries in Figure 21b also correspond fairly well. The initial contraction is slightly overpredicted by the Kocurek-Tangler prescribed wake, while it is slightly underpredicted by the EHPIC analysis. Once again, both models appear to predict the average radial contraction of the tip vortices, but neither model depicts the unsteady characteristics of the wake. At $\Psi_w = 255°$, the measured radial coordinates of the rotor wake deviate about 0.05R of the nominal value as predicted by both wake models. By a complete rotor revolution ($\Psi_w = 360°$), the radial coordinates deviate as much as 0.09R.

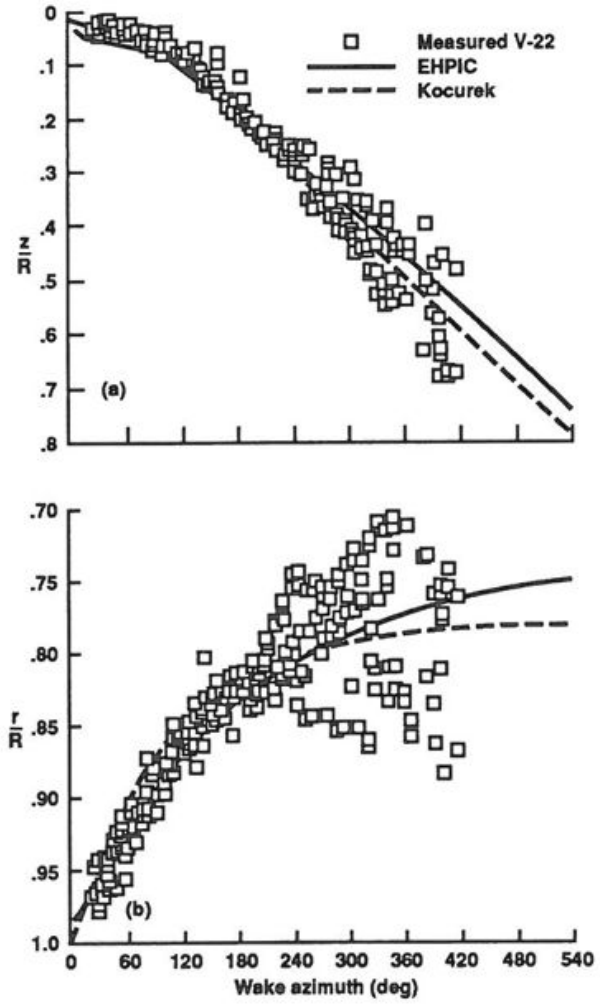

Figure 21. Experimental and predicted V-22 wake geometries; a) axial, b) radial

Isolated Rotor Performance

Comparisons were also made between the 0.184-scale and 0.658-scale V-22 (Ref. 20) isolated tiltrotor performance. Differences in rotor performance were evident at the higher thrust conditions (Fig. 22). This was probably due to Reynolds number effects and the fact that only an aerodynamically scaled rotor was tested. Reference 21 emphasized the importance that model rotors be both dynamically and aerodynamically scaled to simulate full-scale rotor performance. These differences may subsequently affect wake structure and core size. To investigate this, it is recommended that flow visualization of a full-scale tiltrotor be done.

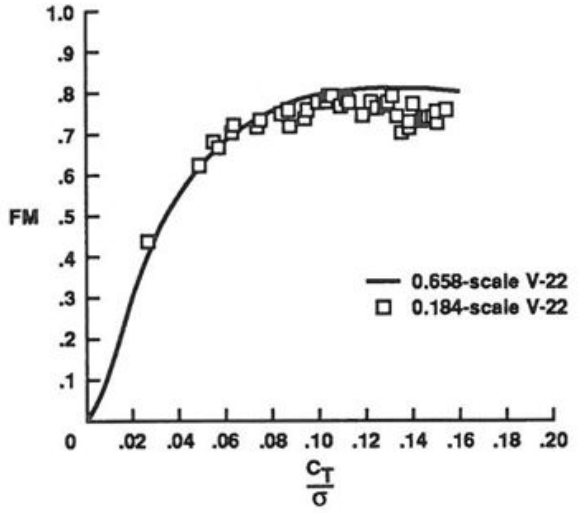

Figure 22. Comparisons between 0.184-scale and 0.658-scale V-22 isolated tiltrotor performance

SUMMARY AND RECOMMENDATIONS

A shadowgraph test was conducted to examine the tip vortex geometry and wake structure of a tiltrotor and wing in hover. The following results were found:

1) Quantitative shadowgraph measurements were made of the visible tiltrotor tip vortex core. Although no velocimetry was conducted, measurements from this test strongly indicate the vortex core is sensitive to thrust and wake age. A linear relationship was found between core measurements and increasing thrust condition. Core measurements also increased with increasing wake age.

2) Fluctuations in the inherently unsteady wake of the tiltrotor appear as scatter in the data. The radial tip vortex geometry is very unsteady at high thrust conditions and clearly exhibits an asymmetric behavior after the first and second blade passages. Tip vortex distortion and wake boundary expansion were more visible on one side of the rotor—the side where the blade approaches the camera. Similar unsteady and asymmetric wake behavior was seen in rotors with little to no twist (Ref. 9).

3) The presence of the wing contributes primarily to the radial expansion of the rotor wake. This agrees with the results acquired in Reference 5.

4) The presence of the image plane significantly contributes to the radial expansion of the wake and illustrates the recirculation region known as the fountain effect. The image plane also affected the rotor performance and reduced the effective thrust of the rotor by 5% for a collective pitch of 13°. This reduction in thrust is apparently due to the recirculation of the rotor downwash, which affects the rotor inflow, and reduces the effective angle of attack of the rotor.

5) Both the Kocurek-Tangler and EHPIC wake models adequately predict the average axial and radial tip vortex coordinates for the V-22 tiltrotor. Because of the unsteady nature of the wake, it is difficult to tell if either model is significantly better. These experimental data suggest that improvements could be made to existing prescribed-wake and free-wake models by incorporating the unsteady nature of the wake and modeling the tip vortex by how much it deviates from its nominal trajectory.

6) Finally, further study should be done to relate core measurements with maximum tangential velocity by conducting concurrent velocimetry and flow visualization studies (such as the wide-field shadowgraph technique). Measurements should be made at close range in order to examine the intricate detail and size of the vortex core. If the shadowgraph technique proves to be an accurate means of measuring core size, it would be very beneficial because it is non-intrusive and allows instantaneous examination of the flow field.

REFERENCES

1. Felker, F. F., Maisel, M. D., and Betzina, M. D., "Full Scale Tilt Rotor Hover Performance," *Proceedings of the 41st Annual Forum of the American Helicopter Society*, Fort Worth, Texas, May 1985.

2. Landgrebe, A., "The Wake Geometry of a Hovering Rotor and its Influence on Rotor Performance," *Journal of the American Helicopter Society*, Vol. 17, No. 4, Oct. 1972.

3. Kocurek, J. and Tangler, J., "A Prescribed Wake Lifting Surface Hover Performance Analysis," *Journal of the American Helicopter Society*, Vol. 22, No. 1, Jan. 1977.

4. Felker, F. F. and Light, J. S., "Aerodynamic Interactions Between a Rotor and Wing in Hover," *Journal of the American Helicopter Society*, Vol. 33, No. 2, April 1988.

5. Norman, T. and Light, J., "Rotor Tip Vortex Geometry Measurements Using the Wide-Field Shadowgraph Technique," *Journal of the American Helicopter Society*, Vol. 32, No. 2, April 1987.

6. Coffen, D. C., George, A. R., Hardinge, H., and Stevenson, R., "Flow Visualization and Flow Field Measurements of a 1/12 Scale Tilt Rotor Aircraft in Hover," *Proceedings of the International Technical Specialists Meeting Rotorcraft Acoustics and Rotor Fluid Dynamics*, Philadelphia, Pennsylvania, Oct. 1991.

7. Parthasaraty, S. P., Cho, Y. I., and Back, L. H., "Fundamental Study of Flow Field Generated by Rotorcraft Blades Using Wide-field Shadowgraph," AIAA-85-1557, *18th AIAA Fluid Dynamics and Plasmadynamics and Lasers Conference*, Cincinnati, OH, July 1985.

8. Merzkirch, W., "Flow Visualization," Academic Press, Inc., NY, 1974, pp. 76-86.

9. Light, J., "Tip Vortex Geometry of a Hovering Helicopter Rotor in Ground Effect," *Proceedings of the 45th Annual Forum of the American Helicopter Society*, Boston, MA, May 1989.

10. Johnson, W., Helicopter Theory, Princeton University Press, Princeton, NJ, 1980, pp. 76, pp. 536-540.

11. Tung, C., Pucci, S. L., Caradonna, F. X., and Morse, H. A., "The Structure of Trailing Vortices Generated by Model Rotor Blades," *Proceedings of the Seventh European Rotorcraft and Powered Lift Aircraft Forum*, Sept. 8-11, 1981, Garmisch-Partenkirchen, F.R.G.

12. Hoffman, E. R. and Joubert, P. N., "Turbulent Line Vortices," *Journal of Fluid Mechanics*, 16, Part 3, 1963.

13. Saffman, P. G., "Structure of Turbulent Line Vortices," Physics Fluids 16(8), 1973.

14. Leishman, J. G. and Bagai, A., "Fundamental Studies of Rotor Wakes in Low Speed Forward Flight using Wide-Field Shadowgraphy," *Proceedings of the AIAA 9th Applied Aerodynamics Conference*, Baltimore, MD, Sept. 23-26, 1991.

15. Beddoes, T. S., "A Wake Model for High Resolution Airloads," *Proceedings of the 2nd International Conference on Basic Rotorcraft Research*, Triangle Park, NC, 1985.

16. Scully, M. P., "Computation of Helicopter Rotor Wake Geometry and Its Influence on Rotor Harmonic Airloads," Massachusetts Institute of Technology ASRL TR 178-1, Mar. 1975.

17. Quackenbush, T., Bliss, D., Wachspress, D., and Ong, C., "Free Wake Analysis of Hover Performance Using a New Influence Coefficient Method," NASA Contractor Report 4150, 1988.

18. Quackenbush, T. and Wachspress, D., "Enhancements to a New Free Wake Hover Analysis," NASA Contractor Report 177523, 1989.

19. Felker, F., Quackenbush, T., Bliss, D., and Light, J., "Comparisons of Predicted and Measured Rotor Performance in Hover using a New Free Wake Analysis," Vertica, Vol. 14, No. 3, 1990.

20. Felker, F. F., Signor, D. B., Young, L. A., and Betzina, M. D., "Performance and Load Data From a Hover Test of a 0.658-Scale V-22 Rotor and Wing," NASA Technical Memorandum 89419, April 1987.

21. Keys, C. N., McVeigh, M. A., Dadone, L., and McHugh, F. J., "Estimation of Full-Scale Rotor Performance from Model Rotor Test Data," *Journal of the American Helicopter Society*, Vol. 30, No. 4, Oct. 1985.